npj | computational materials

Article

Published in partnership with the Shanghai Institute of Ceramics of the Chinese Academy of Sciences

https://doi.org/10.1038/s41524-025-01632-3

Importance of enforcing Hund's rules in density functional theory calculations of rare earth magnetocrystalline anisotropy

Y. Lee[1], Z. Ning[1], R. Flint[1,2], R. J. McQueeney[1,2], I. I. Mazin[3,4] & Liqin Ke[1]

Density functional theory (DFT) and its extensions, such as DFT+U and DFT+dynamical mean-field theory, are invaluable for studying magnetic properties in solids. However, rare-earth (R) materials remain challenging due to self-interaction errors and the lack of proper orbital polarization. We show how the orbital dependence of self-interaction error contradicts Hund's rules and plagues magnetocrystalline anisotropy (MA) calculations, and how analyzing DFT states that respect Hund's rules can mitigate this issue. We benchmark MA in RCo$_5$, R_2Fe$_{14}$B, and RFe$_{12}$, extending prior work on RMn$_6$Sn$_6$, achieving excellent agreement with experiments. Additionally, we illustrate a semi-analytical perturbation approach that treats crystal fields as a perturbation in the large spin-orbit coupling limit. Using Gd-4f crystal-field splitting, this method provides a microscopic understanding of MA and enables rapid screening of high-MA materials.

Among all the elements, the open-shelled lanthanides provide the largest magnetocrystalline anisotropy (MA), due to the strongly-localized nature of 4f orbitals and strong spin-orbit coupling (SOC), which can evolve substantially, including changing sign while varying the rare earth (R) element in an isostructural series of compounds. The unparalleled strength and tunability of rare-earth MA allows for a wide range of applications, ranging from conventional high-performance permanent magnets[1–4] to recent rare-earth-containing topological magnets[5,6]. To further exploit existing systems and explore new ones, ab initio methods that can provide a microscopic understanding of rare-earth anisotropy and reliably predict new materials are highly desired.

The MA originates from the interplay between SOC and the crystal field (CF)[7,8]. The 4f states are the *most-localized* among all shells and generally well-shielded by the outermost electrons, resulting in a small CF splitting (Δ) of tens of meV. Considering the relatively large SOC strength ξ, CF effects can be treated as a perturbation, and the 4f orbital largely remains atomic-like. The mechanism of R MA can be understood in the following picture. When the spin of 4f electrons rotates, in the first approximation, the charge of the strongly-correlated 4f electrons remains the same shape and follows the spin, as the spin and orbitals are locked by the large SOC. The MA then arises from the energy variation corresponding to the rotating aspherical 4f cloud under the ligand-induced CF potential. In the conventional CF theory, this energy dependence on spin direction (θ, ϕ) can be written as:

$$E(\theta,\phi)=\int \mathrm{d}\mathbf{r}\rho_{4f}(\mathbf{r};\theta,\phi)V_{\mathrm{CF}}(\mathbf{r})=\sum A_l^m Q_l^m(\theta,\phi). \quad (1)$$

Here, the CF potential of isostructural compounds is characterized by CF parameters (CFPs) A_l^m, while the asphericity of the rotating 4f charge, evolved with 4f orbital filling, is characterized by multipole moment $Q_l^m(\theta,\phi)$. The multipole moment can be expressed in terms of the Stevens coefficients Θ_l, the operator equivalents $\mathcal{O}_l^m$, and the rare-earth radii $\langle r^l\rangle_{4f}$, e.g., $Q_l^0=\Theta_l\langle r^l\rangle_{4f}\mathcal{O}_l^0$[9–11]. Overall, the 4$f$ electron configurations in solids, especially those of heavy R elements, generally obey the same Hund's rules as in a free ion, according to the so-called standard rare-earth model (SRM)[12–14]. The MA of 4f elements can reach the same order of magnitude as the CF strength, which typically ranges in tens of meV.

The atomic nature of the strongly-correlated, localized 4f electrons poses great challenges for mean-field methods such as density functional theory (DFT). Various approaches, including the 4f-open-core method, DFT+U[6,15], dynamical mean-field theory (DMFT)[16,17], and quasiparticle self-consistent GW (QSGW)[18], have been employed depending on the specific rare-earth properties being targeted. DFT+U is the simplest and

[1]Ames National Laboratory, U.S. Department of Energy, Ames, IA, USA. [2]Department of Physics and Astronomy, Iowa State University, Ames, IA, USA. [3]Department of Physics and Astronomy, George Mason University, Fairfax, VA, USA. [4]Quantum Science and Engineering Center, George Mason University, Fairfax, VA, USA. e-mail: liqinke@ameslab.gov

most widely-used method to treat strong correlations. Regarding the 4*f* MA, the primary issue with DFT+*U* is that it is known to fail in reproducing the experimental ground-state 4*f* configuration[15,19–24]. Specifically, it fails to reproduce Hund's second rule, which maximizes orbital polarization.

In general, DFT+*U* can have many metastable 4*f*-configuration solutions[13,24,25], and the correct *ground state* often appears in DFT+*U* as a *metastable* state that is hundreds of meV higher. As discussed in detail, for instance, in ref. 24, the root of the problem is the orbital-dependent self-interaction error (SIE), stemming from the fact that each Kohn-Sham particle interacts with the *total* charge density, including its own. This orbital dependence of SIE is particularly significant for 4*f* orbitals, leading to incorrect orbital occupancies and 4*f* charge density, and consequently to incorrect MA.

A key question arises: *Can DFT+U accurately describe the MA of tens of meV, even though it overestimates the energy of the true ground state by hundreds of meV?* Our recent systematic study on topological magnetic compounds RMn$_6$Sn$_6$ with heavy-R elements has shown promise[6], provided that their Hund's-rules ground states are enforced. Not only are the easy directions of the entire series of compounds reproduced if Hund's rules are enforced[6], but the calculated MAE amplitude also agrees reasonably well with experiments[26,27]. However, it remains unclear how well the delicate MA in other rare-earth-containing magnets can be described using the SRM in the simplistic DFT+*U* framework. To better establish the validity and effectiveness of these methods, systematic investigations of MA in more rare-earth-based compounds are needed.

In this work, we first review and illustrate how the orbital dependence of SIE affects the 4*f* ground state and MA calculation in DFT-based methods. We then discuss various methods that attempt to enforce Hund's rules, such as DFT+*U*, self-interaction corrections (SIC), and orbital polarization corrections (OPC), and how the additional terms therein affect the MA calculations. We further systematically benchmark DFT+*U* calculations of MA in several isostructural *R*-transition-metal (*R*-TM) intermetallic series, including well-established permanent magnet systems, RCo_5, $R_2Fe_{14}B$, and RFe_{12} with heavy *R* elements. In all cases, with the enforcement of Hund's rules, DFT+*U* calculations provide a useful description of the MA without the need to include SIC and OPC. Finally, we demonstrate that the evolution of MA can be modeled analytically based on a perturbative treatment of the crystal field using the single-particle 4*f* levels obtained in DFT+*U*[6].

Results

SIE effects on 4f Ground state and MA in DFT: TbMn$_6$Sn$_6$ as an example

Many-body effects are crucial for accurately describing the strongly-correlated 4*f* electrons. Especially for light rare-earth elements, multiple Slater determinants are typically required to capture their complex electronic structure. Here, in this study, we focus primarily on the heavy *R* elements with a large *R*-TM exchange coupling because their ground states effectively satisfy Hund's rules, and the $|L, S, J, m_J = J\rangle$ state with $J = L + S$ can, in principle, be represented using a single Slater determinant, as in methods such as DFT[28]. However, even for these "relatively easier" heavy-*R* cases, challenges arise in describing 4*f* electrons, specifically related to the SIE and the corresponding violation of Hund's rules.

To gain a quantitative understanding of how SIE affects the ground state and MA, we illustrate this with a DFT+U calculation of TbMn$_6$Sn$_6$-a recently discovered quantum magnet with very strong easy-axis anisotropy. According to Hund's rules, Tb^{3+} ($4f^8$) is expected to have a fully-filled 4*f* majority-spin channel and one electron in the minority spin channel, with $4f^{1,\downarrow}_{|m_l=3\rangle}$. This expectation is consistent with neutron scattering and magnetization measurements of TbMn$_6$Sn$_6$[26] and TbV$_6$Sn$_6$[27]. However, DFT+*U* instead found a 4*f* ground state corresponding to $4f^{1,\downarrow}_{|m_l=2\rangle}$[6,27]. The experimental ground state is approximately $\Delta\epsilon$ = 340 meV higher in TbMn$_6$Sn$_6$, appearing as a metastable state in DFT+*U* (performed with SOC included and the experimental out-of-plane spin orientation at U = 10 eV).

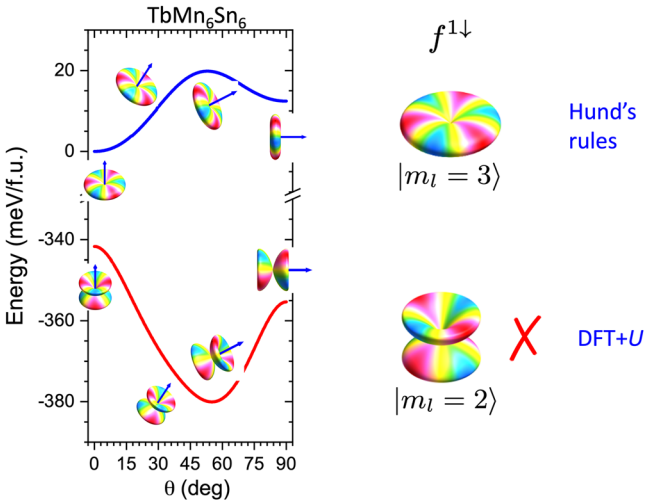

Fig. 1 | Magnetocrystalline anisotropy in TbMn$_6$Sn$_6$, represented by the variation of magnetic energy as a function of spin-axis rotation, calculated using DFT+*U*. The true ground state of Tb^{3+} ($4f^8 = 4f^{7\uparrow} + 4f^{1\downarrow}$), following Hund's rules, appears as a metastable state in DFT+*U*. The anisotropy calculated for two configurations, the true ground state $4f^{1,\downarrow}_{|m_l=3\rangle}$ and the DFT+*U* ground state $4f^{1,\downarrow}_{|m_l=2\rangle}$, is represented by the blue and red lines, respectively. The two $4f^{1,\downarrow}$ configurations are illustrated with polar plots of the corresponding complex spherical harmonics $Y^m_{l=3}(\theta, \phi)$, where the radius represents the amplitude and the color represents the phase at the point (θ, ϕ).

Considering that the SOC included in calculation already lowers the $|3\rangle$ state relative to $|2\rangle$ by approximately $\frac{1}{2}\xi^{Tb}_{4f} \approx 120$ meV, the orbital dependence of SIE for these two orbitals is about 460 meV, which is more than one order of magnitude larger than MA.

The SIE, while sizable, is practically independent of the crystallographic environment and is rotationally invariant. The energy difference between these two 4*f* configurations remains essentially the same as for the free Tb^{3+} ion, where we found $\Delta\epsilon_{atom}$ = 350 meV using a large supercell calculation. Moreover, to ensure numerical accuracy, we calculated the variation of $\Delta\epsilon_{atom}$ with spin rotation and found that the change is negligible. In other words, the SIE is spin-rotationally invariant.

If, as we just established, the SIE is rotationally invariant, one may work around that by calculating the MA (and similar effects) not in the DFT ground state, but in a metastable state that respects Hund's rules. This can be achieved by starting DFT+U calculations from a 4*f* occupation matrix constructed according to the desired orbital state, and by monitoring and controlling the orbital occupancy through the self-consistency process to ensure convergence closely to the targeted state. Such capability is easy to implement and is generally available in popular DFT packages, including WIEN2K and VASP[29].

Figure 1 shows the total energy variation as a function of the spin-quantization axis rotation, characterized by polar angle θ, calculated for the two 4*f* configurations corresponding to the experimental and DFT ground states, respectively. As illustrated in Fig. 1, at each polar angle, using the procedure discussed above, the calculations converge to solutions closely approximating the $4f^{1,\downarrow}_{|m_l=3\rangle}$ and $4f^{1,\downarrow}_{|m_l=2\rangle}$ configurations, respectively, in the local coordinate system (with the *z*-axis along the spin direction). The MA profiles calculated with these two solutions are markedly different. Calculations using the $|m_l = 2\rangle$ DFT+U ground state yield an incorrect easy-cone MA, while those calculated with the $|m_l = 3\rangle$ configuration, the true ground state but metastable in DFT+U calculations, correctly host a strong easy-axis MA.

This is not surprising, as the $|m_l = 2\rangle$ and $|m_l = 3\rangle$ configurations lead to different asphericities of the 4*f* charge distribution, or equivalently, different multipole moments Q_b, which result in drastically different MA.

Therefore, for accurate MA calculations, it is crucial to enforce solutions that represent the correct 4*f* orbital configurations.

Origin of erroneous Tb-4*f* ground state: orbital dependence of SIE

The origin of the erroneous $f^{1,\downarrow}_{|m_l=2\rangle}$ ground state in DFT calculations for the Tb^{3+} ion is due to the strong orbital dependence of the SIE for 4*f* orbitals. The Tb^{3+} atom, with a $4f^8$ configuration, has a fully-occupied 4*f* majority-spin channel that produces an *s*-type spherical charge and potential. In a single-particle Hamiltonian, without considering SOC, the seven 4*f* states should be degenerate if the potential is orbital-independent, as in plain DFT, and spherical. Therefore, excluding self-interaction, the additional electron in the minority-spin channel, $f^{1,\downarrow}$, experiences a nearly spherical potential that does not lift the degeneracy of the seven 4*f* orbital states. This is the same reason behind the well-known issue of 4*f* states being pinned at the Fermi level in DFT calculations unless a sizable Hubbard *U* interaction is introduced in schemes such as DFT +U to polarize the occupied and unoccupied 4*f* states. However, in DFT, the occupied $f^{1,\downarrow}$ electron generates an aspherical charge density that acts upon itself, as the functionals are evaluated using the total electron density. The total SIE in the local density approximation (LDA), ϵ^{LDA}, originates from the Hartree energy, E_{H}, and the exchange-correlation energy, E_{xc}, and can be written as

$$\epsilon^{\mathrm{LDA}} = \epsilon^{\mathrm{H}} + \epsilon^{\mathrm{xc}}, \tag{2}$$

where ϵ^{H} and ϵ^{xc} are the corresponding SIE contributions associated with E_{H} and E_{xc}, respectively. Due to the local approximation of the unknown exact exchange-correlation functional, ϵ^{H} and ϵ^{xc} do not cancel out as ϵ^{H} and ϵ^{x} (self-exchange) do in the Hartree-Fock method, resulting in a nonzero ϵ^{LDA}. Moreover, the orbital dependence of ϵ^{LDA} is substantial for 4*f* states, leading to an incorrect 4*f* ground state.

Since the 4*f* charge asphericity and orbital dependence of SIE for the Tb^{3+} ion (with $f^{7,\uparrow} + f^{1,\downarrow}$ configuration) are predominantly associated with the single electron in the minority-spin channel, we now present an analytical estimation of ϵ^{H} and ϵ^{xc} for the f^1 configurations with various $|m_l\rangle$ states. Obviously, we have $\epsilon^{\mathrm{H}} = E_{\mathrm{H}}$ and $\epsilon^{\mathrm{xc}} = E_{\mathrm{xc}}$ for this single-electron model. Here, we consider the eigenstates of the *f* electron, where the angular part of the wavefunction is described by complex spherical harmonics $Y^m_{l=3}$. As we will show, ϵ^{H} favors the $|m_l = 2\rangle$ state, with the energy order $|2\rangle < |1\rangle < |3\rangle < |0\rangle$. Conversely, ϵ^{xc} favors the $|m_l = 0\rangle$ state, with the energy hierarchy $|2\rangle > |1\rangle > |3\rangle > |0\rangle$. However, these contributions do not cancel each other out, resulting in an overall ϵ^{LDA} that disfavors the $|m_l = 3\rangle$ state.

Hartree self-interaction for f^1. For the f^1 single-electron state, the ϵ^{H} of the $|\pm m\rangle$ state can be written as:

$$\epsilon^{\mathrm{H}}_m = \frac{1}{2}\iint \mathrm{d}\mathbf{r}_1\, \mathrm{d}\mathbf{r}_2\, \frac{\rho_m(\mathbf{r}_1)\rho_m(\mathbf{r}_2)}{|\mathbf{r}_1 - \mathbf{r}_2|}, \tag{3}$$

where the electron density can be expressed in terms of the radial and angular parts of the wavefunction as $\rho_m(\mathbf{r}) = R^2_{4f}(r)|Y_{3m}(\theta,\phi)|^2$, with $m \in 0, 1, 2, 3$. The Coulomb interaction can be expanded using complex spherical harmonics as:

$$\frac{1}{|\mathbf{r}_1 - \mathbf{r}_2|} = \sum_{k=0}^{\infty} \frac{r^k_<}{r^{k+1}_>} \frac{4\pi}{2k+1} \sum_{q=-k}^{q=k} Y_{kq}(\theta_1,\phi_1) Y^*_{kq}(\theta_2,\phi_2), \tag{4}$$

Table 1 | The coefficients a_{mk}, where *m* denotes the complex spherical harmonics

m	a_{m2}	a_{m4}	a_{m6}	$\tilde{a}_{m2}$	$\Delta\epsilon^{\mathrm{H}}_m$
0	0.0711	0.0331	0.0543	0.1201	876
± 1	0.0400	0.0009	0.0306	0.0557	232
± 2	0	0.0450	0.0049	0.0325	0
± 3	0.1111	0.0083	0.0001	0.1167	842

The coefficients $\tilde{a}_{m2} = a_{m2} + 0.6681a_{m4} + 0.4943a_{m6}$ is calculated by assuming the ratio between F_2, F_4, and F_6 values as 1: 0.6681: 0.4943. The orbital-dependent part of ϵ^{H}_m, $\Delta\epsilon^{\mathrm{H}}_m$ (in units of meV), is then calculated by further assuming $F_2 = 10$ eV, with the value of the $|\pm 2\rangle$ state as the reference zero. For complex $|m\rangle$ states, the ordering is $|\pm 2\rangle < |\pm 1\rangle < |\pm 3\rangle < |0\rangle$.

where $\mathbf{r}_i = r_i(\sin\theta_i\cos\phi_i, \sin\theta_i\sin\phi_i, \cos\theta_i)$, and $r_< = \min(r_1, r_2)$ and $r_> = \max(r_1, r_2)$.

Substituting Eq. (4) into Eq. (3) and separating the radial and angular parts of the integration, we obtain:

$$\begin{pmatrix}\epsilon_0\\ \epsilon_1\\ \epsilon_2\\ \epsilon_3\end{pmatrix}^{\mathrm{H}} = F_0 + \begin{pmatrix} a_{02} & a_{04} & a_{06}\\ a_{12} & a_{14} & a_{16}\\ a_{22} & a_{24} & a_{26}\\ a_{32} & a_{34} & a_{36}\end{pmatrix}\begin{pmatrix}F_2\\ F_4\\ F_6\end{pmatrix} \approx F_0 + \begin{pmatrix}\tilde{a}_{02}\\ \tilde{a}_{12}\\ \tilde{a}_{22}\\ \tilde{a}_{32}\end{pmatrix} F_2. \tag{5}$$

Here, the radial integrals are represented by the Slater integrals [F_0, F_2, F_4, F_6], and the angular integrals are represented by the matrix element a_{mk}, which can be evaluated using the Gaunt coefficients as follows:

$$a_{mk} = \frac{4\pi}{2k+1}[\mathrm{Gaunt}\,(3, \mathrm{k}, 3; -\mathrm{m}, 0, \mathrm{m})]^2. \tag{6}$$

The last step of Eq. (5) is obtained using $a_{m0} = 1$ and assuming $F_4/F_2 \approx 0.6681$ and $F_6/F_2 \approx 0.4943$.

Table 1 lists the matrix elements a_{mk} and the effective element $\tilde{a}_{m2}$, as well as the orbital-dependent part of ϵ^{H}_m, $\Delta\epsilon^{\mathrm{H}}_m \approx \tilde{a}_{m2}F_2$, calculated with $F_2 =$ 10 eV, with respect to the $|m_l = 2\rangle$ state. Clearly, ϵ^{H} favors $|m_l = \pm 2\rangle$ states while disfavoring $|m_l = 0\rangle$ and $|m_l = \pm 3\rangle$ states. The small SIE of $|\pm 2\rangle$ is due to the vanishing of the matrix element a_{22} calculated using Eq. (6), which results from the fact that they satisfy one of the conditions for non-trivial zeros of Wigner-3*j* symbols, i.e., Wigner3j(3, *k*, 3; *m*, 0, − *m*) = 0 with *k* = 2.

Exchange-correlation self-interaction for f^1. The ϵ^{xc}, which comprises the exchange part ϵ^{x} and the correlation part ϵ^{c}, is also orbital-dependent. In general, the exchange energy has a much larger magnitude than the correlation energy, making it the dominant contribution to ϵ^{xc}. With the LDA exchange energy given by $E_{\mathrm{x}}[\rho] \propto -\int \rho^{\frac{4}{3}}(\mathbf{r}), \mathrm{d}r$, the orbital-dependent ϵ^{x}_m for the $f^1 = |\pm m\rangle$ states can be characterized by the angular part of the integration:

$$\Omega(\epsilon^{\mathrm{x}}_m) = -\int \mathrm{d}\theta\mathrm{d}\phi\big(|Y_{lm}(\theta,\phi)|^2\big)^{\frac{4}{3}}. \tag{7}$$

Table 2 lists $\Omega(\epsilon^{\mathrm{x}}_m)$ values and the corresponding values with respect to the $|m = 0\rangle$ state, along with the relative exchange-correlation energy E^{xc}_m and total energy E^{Tot}_m of free Tb atoms calculated using DFT+*U*. Clearly, ϵ^{x}_m favors the $|0\rangle$ minority-spin state, following the energy ordering $|0\rangle < |\pm 3\rangle < |\pm 1\rangle < |\pm 2\rangle$. Numerically, our DFT+*U* calculations for the Tb^{3+} free ion also show that E_{xc} strongly favors $|0\rangle$ state while least favoring $|2\rangle$ state, in agreement with $\Delta\Omega(\epsilon^{\mathrm{x}}_m)$.

Moreover, the numerical values of $E^{\mathrm{Tot}}_m - E^{\mathrm{xc}}_m$ listed in Table 2 follow the same ordering as $\Delta\epsilon^{\mathrm{H}}_m$ listed in Table 1. Therefore, the DFT+*U* calculations provide numerical support for the analytical f^1 model, despite the latter being a highly simplified representation of the Tb^{3+}-4*f* system, which

Table 2 | Angular part of the integration of ϵ^x, denoted as $\Omega(\varepsilon_m^x)$, for the f^1 configuration, along with the exchange-correlation energy E_m^{xc} and total energy E_m^{Tot} of free Tb atoms calculated using DFT+U

m	0	±1	±2	±3
$\Omega(\epsilon_m^x)$	−0.5314	−0.4903	−0.4801	−0.4963
$\Delta\Omega(\epsilon_m^x)$	0	0.0411	0.0513	0.0351
E_m^{xc} (meV)	0	406.1	757.3	689.0
E_m^{Tot} (meV)	0	32.9	73.2	497.4

$\Delta\Omega(\epsilon_m^x)$ represents the $\Omega(\epsilon_m^x)$ values relative to the $|m=0\rangle$ state. Similarly, Tb E_m^{xc} and E_m^{Tot} are calculated relative to the $|m=0,\downarrow\rangle$ state. SOC is not included in the DFT+U calculations.

contains many electrons beyond the single 4f electron in the minority-spin channel.

Overall, when combining ϵ^H and ϵ^{xc}, the total ϵ^{LDA} yields a much higher energy for $|\pm3\rangle$ solutions compared to other $|m\rangle$ solutions. Specifically, ϵ^H strongly favors $|\pm2\rangle$ much more than $|0\rangle$ and $|\pm3\rangle$, while ϵ^{xc} strongly favors $|0\rangle$. Consequently, overall ϵ^{LDA} results in a significantly higher energy for $|\pm3\rangle$ states than for other states. The SOC energy, on the other hand, favors states with large positive m_l values in the minority-spin channel. While it may not be sufficient to overcome the SIE to stabilize the true ground state of $|3\rangle$, it does lower the energy of the $|2\rangle$ state below that of the $|0\rangle$ and $|1\rangle$ states, ultimately leading to an erroneous ground state of $f^{1,\downarrow}_{|m_l=2\rangle}$ in calculations.

DFT+U, DFT+DMFT, SIC, and OPC

Various methods have been developed and employed to improve the DFT description of 4f electrons, including DFT+U, SIC, and OPC methods. Both SIC[30] and OPC[31] methods can be connected to the more general DFT+U method; all of these methods polarize selected local orbitals using an additional orbital-dependent potential within the single-particle DFT framework. DFT+DMFT, on the other hand, enables a multiple-Slater-determinant description of the 4f shell. In this section, we discuss their applications to MA calculations.

DFT+U approach. To resolve the unphysical pinning of 4f states near the Fermi level in DFT, DFT+U with a sizable Hubbard U value is the most employed method to treat the well-localized 4f orbitals, shifting the occupied and unoccupied 4f states away from the Fermi level by $\pm\frac{1}{2}(U-J_H)$, respectively.

The DFT+U total energy, which differs from the plain DFT one by a correlation contribution from the Hubbard-type model Hamiltonian for the selected orbitals, can be written as

$$E_{LDA+U}[\rho(\mathbf{r}),\mathbf{n}] = E_{LDA}(\rho) + E^{corr}(\mathbf{n}), \tag{8}$$

where the correlation energy is evaluated using the occupation matrix $\mathbf{n}$ with the screened Coulomb interactions parameterized with U and J values as

$$E^{corr}(\mathbf{n}) = E^{Hub}(\mathbf{n}) - E_{dc}(n). \tag{9}$$

Here, the Hartree-Fock-like interaction $E^{Hub}(\mathbf{n})$ is self-interaction-free as the SIE of the direct and exchange terms is exactly canceled out[22]; the double-counting term $E_{dc}(n)$, which accounts for the interaction already included in LDA, is not uniquely defined and depends on the implementation scheme. Typically, it depends only on the trace of $\mathbf{n}$; therefore, $E_{dc}(n)$ depends only on the number, but not the orbital character m_l, of the occupied states. It is worth noting that, besides of the aforementioned splitting between the occupied and unoccupied 4f states by $(U-J_H)$, in the popular fully-localized-limit (FLL) double-counting scheme, J_H also induces the spin splitting of corresponding 4f levels, depending on the orbital's occupancy. Overall, the $E^{corr}(\mathbf{n})$ in DFT+U, which consists of the SIE-free $E^{Hub}(\mathbf{n})$ and the orbital-independent $E_{dc}(n)$, do not explicitly address the orbital dependence of SIE. Therefore, the SIE inherited from the original DFT in DFT+U remains largely intact, and conventional DFT+U schemes are not expected to correct the Tb^{3+} ground state discussed above.

Alternative DFT+U schemes that aim to minimize the orbital dependence of SIE have been proposed. An interesting work by Zhou and Ozoliņš modifies only the exchange term of the LDA by including only the exchange, but not Hartree, component of $E^{corr}(\mathbf{n})$. The exchange-only $E^{corr}(\mathbf{n})$ now contains orbital-dependent SIE and can be used to minimize the orbital dependence of SIE by properly mixing the FLL $E_{dc}(n)$ exchange and LDA exchange. This method has been demonstrated to improve the description of the 4f ground-state and other properties such as CFP and optical properties[24,32]. However, such corrections, with rotational invariant $E^{corr}(\mathbf{n})$, does not explicitly affect the calculated $E(\theta,\phi)$ profile once the 4f configuration is enforced during the rotation.

Therefore, the main effect of applying the U parameter is to shift the occupied 4f states away from the Fermi level. This shift is necessary to be consistent with experiments and helps ensure convergence to the desired 4f orbital occupation that respects all three Hund's rules, which may otherwise be disrupted by strong hybridization between 4f and ligand orbitals. This is because, when the spin-quantization axis rotates, the U- and J_H-dependent correlation energy remains constant as long as the orbital occupancy remains the same in the local coordinate system. On the other hand, in the range of U values that lead to strong hybridization between 4f and ligand orbitals, a much stronger U dependence of MA is expected. This is because the contribution of hybridization, in addition to the crystal electric field, becomes more significant for MA.

DFT+DMFT approach. In contrast to DFT+U, where the Hubbard-type interaction is treated by adding a Hartree-Fock-like mean-field term into the LDA Hamiltonian, DMFT allows a multiconfigurational description for the selected orbitals of rare-earth elements, capturing the atomic physics of the 4f shell. Applications to rare-earth elements so far have mostly been implemented using the Hubbard-I approximation (HIA)[33], which neglects the explicit hybridization between the impurity and the bath for simplicity and computational efficiency. DFT+HIA has been used to investigate various properties of rare-earth materials, including cohesive, structural, spectroscopic, and magnetic properties[13,14]; it has later been extended to more challenging properties such as magnetocrystalline anisotropy and crystal-field parameters[16,17,34], with further development of methods and implementations, e.g., the implementation of a charge self-consistency scheme[35]. An advantage of DMFT over DFT+U is its improved description of correlation effects. However, the principal problem outlined above—the SIE of the 4f-orbitals—remains equally severe in DFT+DMFT as in DFT+U. In ref. 16, this issue was circumvented in an ingenious way: they replaced the actual 4f-electron density obtained in DMFT with its spherical average by enforcing a uniform occupancy of the 4f ground-state multiplet before recalculating the electron density and updating the one-electron Kohn-Sham potential in the next DFT iteration. Conceptually, this approach is similar to our analytical model, which replaces the crystal field of an actual material with that of spherically symmetric Gd, as described below. However, it contrasts with our ab initio calculation, where the crystal fields and hybridizations effects on MA are evaluated based on the charge density with properly-enforced Hund's-rules 4f occupations.

Self-interaction correction. The SIC method, proposed by Perdew and Zunger in 1981[36], was initially inspired by the problem of reproducing the correct energy gap in insulators. They pointed out that in the limit of one-electron systems, the exchange-correlation potential should exactly cancel the Hartree potential, which was not the case for all functionals available at that time. With this in mind, Perdew and Zunger proposed a method that deducts the self-interaction energy of each orbital from the DFT functional. The resulting orbital-dependent functional was neither a Kohn-Sham functional nor uniquely defined for many-electron

systems[36–39]. Nevertheless, it was conceived that this functional would offer a better approximation to the exact Kohn-Sham functional than existing local flavors. However, it was never proven to systematically improve the total energy. Indeed, the weighted density functional[40], which is inherently self-interaction-free in the Perdew-Zunger sense and yields improved total energy and linear response[41], produces results that are quite different from those of SIC LDA or GGA functionals.

There have been widespread applications of the SIC method across various materials, including localized 4*f* systems[42]. For instance, Strange et al.[43] demonstrated it to investigate the preferred valence states of *R*-compounds by calculating the energy differences between R^{3+} and R^{2+} states. Hughes et al.[44] utilized SIC to study lanthanide contraction and magnetism in heavy rare-earth elements. Svane et al.[45] demonstrated that the SIC method provides a more accurate description of isostructural transitions, the equilibrium lattice constants of Ce and CeP, and the zero-temperature equations of state for Pr and Sm compared to LDA. Lüders et al.[46] implemented SIC using multiple scattering theory and applied it to the α-γ phase transition in Ce. Patrick et al.[47] utilized SIC with the disordered local moment (DLM) formalism to investigate the finite-temperature magnetic properties of RCo_5. Overall, SIC provides a parameter-free approach to enhancing the localization of correlated orbitals, leading to a more accurate description of various properties.

However, to the best of our knowledge, there is still a lack of systematic studies demonstrating whether the application of SIC can resolve the orbital dependence of 4*f* SIE and correctly reproduce the Hund's rule ground state of 4*f* states in rare-earth magnets. Thus, there is no solid foundation for expecting that such non-DFT SIC functionals would universally enforce Hund's rules in *f*-electron systems, nor is this method (as opposed to DFT+*U*) commonly implemented in modern DFT codes.

Orbital polarization correction. In analogy to the Stoner expression for spin polarization $-\frac{1}{4}IM_s^2$, Brooks and coworkers[48] introduced an orbital polarization term proportional to $-\frac{1}{2}L^2$, giving rise to a one-electron eigenvalue shift ($-E^3Lm_l$) for the state $|m_l\rangle$. Here, the Racah parameter E^3, which can be related to Slater integrals (F_2, F_4, and F_6), plays a role analogous to the Stoner *I* for spin polarization.

While this method does introduce a correction that tries to maximize the orbital moment and, thus, technically can enforce Hund's rules, it has no direct first-principles justification. Various attempts[31,49] to derive an OPC have resulted in formulations that, while potentially useful, differ from the suggested form. To the best of our knowledge, the more elaborate OPC schemes beyond the original description of Brooks and coworkers are neither implemented in standard codes nor universally tested.

The original OPC prescription is implemented in WIEN2K code and we applied it to TbV_6Sn_6. It appears that achieving the Hund's rule state using the OP method is quite challenging, if not impossible. In the minority spin channel, $|m_l = 2\rangle$ levels remain the lowest unless a very high OP parameter is applied to promote the occupation of the $|m_l = 3\rangle$ state. However, since the orbital polarization term is spin-independent, such a large OP parameter also causes large orbital polarization in the majority-spin channel, resulting in partial occupation in the majority-spin channel. As a result, with this OPC scheme, we are not able to obtain the correct 4*f* ground state that satisfies Hund's rules.

Thus, we conclude that neither the SIC nor the OPC method, at least by itself, is useful for extensive calculations of MA in 4*f*-metal compounds. Therefore, we will pursue the idea discussed above of calculating MA in an artificially stabilized, computationally-metastable orbital state that respects Hund's rules.

4*f* anisotropy: Benchmarking total energy calculation

To systematically benchmark the validity of MA calculations, we further investigate several isostructural systems, including the two most important permanent magnet systems: RCo_5 and $R_2Fe_{14}B$. Among them, $SmCo_5$- and Fe-rich $Nd_2Fe_{14}B$-based magnets are the most successful permanent magnets so far. We will show that the rare-earth MA in these systems can be well described using DFT+*U*.

Various methods, including DFT+*U*, SIC[47], and DMFT in the form of Hubbard I[16,17], have been employed to investigate the rare-earth MA in these systems, especially for $SmCo_5$ due to its importance and a smaller RCo_5 unit cell. However, despite the wide application of simplistic DFT+*U*, the systematic MA study of isostructural series with heavy-*R* elements is, to the best of our knowledge, rare. Moreover, most of the previous calculations in the literature did not discuss the details of the converged 4*f* configuration or were carried out without enforcing Hund's rules; the calculated orbital moments can deviate significantly from SRM due to the orbital-dependent SIE in DFT+*U* and the corresponding failure to reproduce Hund's rules being ignored. Consequently, the reported orbital magnetic moment and MA values are scattered and hard to evaluate, casting doubt on the validity of DFT+*U* applications for rare-earth MA.

Therefore, here we want to fill this gap by systematically benchmarking MA calculations with the SRM model using DFT+*U*. Such benchmarking is also necessary if we want to compare with more sophisticated approaches such as DMFT or other methods and evaluate their improvement.

Here, we focus on the rare-earth MA in these systems, although the transition-metal sublattice MA is also important and of interest by itself[50]. For example, in RCo_5, the Co sublattice also contributes a large easy-axis anisotropy, as YCo_5 represents one of the largest 3*d* MA systems. However, plain DFT underestimates the MA of Co sublattices and only gives a value between $\frac{1}{4}$ and $\frac{1}{3}$ of the experimental value in RCo_5[51]. Orbital polarization[34,52] or applying an additional Hubbard *U* interaction on Co-3*d* orbitals in DMFT[53] or DFT+*U* has been used to improve the agreement between calculation and experiments.

***R*Co$_5$ compounds**. Figure 2 shows the calculated total energies $E(\theta, \phi)$ in RCo_5 as functions of spin-quantization direction characterized by the polar angle θ and the azimuthal angle ϕ. Besides the heavy *R* elements, we also consider *R* = Sm and Nd for comparison with existing experimental data. In contrast to other RCo_5 compounds, $GdCo_5$ with a spherical Gd-4*f* charge exhibits a very small easy-axis MA, contributed mostly by the Co sublattices. The energy minimum occurs at $\theta = 0°$, [0 0 1], for Er and Sm, and at $\theta = 90°$ for all other compounds. This suggests that RCo_5 has an easy-axis MA for *R* = Er and Sm, while an easy-plane MA for *R* = Tb, Dy, Ho, and Nd. The calculations for all the compounds accurately reproduce their experimental easy directions measured at low temperatures[54–57], demonstrating the effectiveness of MA description in SRM through DFT+*U*.

$HoCo_5$ shares a similar MA profile with $NdCo_5$ but has an opposite MA profile to $ErCo_5$. This can be understood as Ho^{3+} with a $4f^{3,\downarrow}$ configuration and Nd^{3+} with a $4f^{3,\uparrow}$ configuration having a similar aspherical charge density in the single-Slater-determinant description of DFT, if one ignores the difference between their radial wavefunctions. The nearly perfect opposite MA profiles of $HoCo_5$ and $ErCo_5$ reflect the particle-hole symmetry also found in $HoMn_6Sn_6$ and $ErMn_6Sn_6$[6].

Interestingly, all RCo_5 compounds exhibit a sizable in-plane MA, suggesting a significant higher-order CFP A_6^6. Among all *R* elements, $TbCo_5$ has the smallest in-plane MA, while $NdCo_5$ shows the strongest in-plane MA, almost equal in amplitude to the out-of-plane MA. Notably, a large in-plane MA in $NdCo_5$ has been observed experimentally[58,59] and has also been reproduced in a recent DFT+DMFT study[17]. Assuming a fixed CFP A_6^6 for the isostructural RCo_5, the magnitude of in-plane MA correlates well with the element's multipole moment Q_6, with the largest value found in Nd and the smallest in Tb. However, our calculations overestimate the in-plane anisotropy of $NdCo_5$ due to inherent limitations of DFT, which can be alleviated by employing a multiple-Slater-determinant approach.

It is worth noting that the in-plane MA in $SmCo_5$ would vanish in a conventional CFP model using the lowest multiplet $|L = 5, S = \frac{5}{2}, J = \frac{5}{2}, m_J\rangle$, as the Stevens operator $\mathcal{O}_6^6$ vanishes for $J = \frac{5}{2}$, unless the *J* mixing due to multiplet interaction is considered. The non-zero

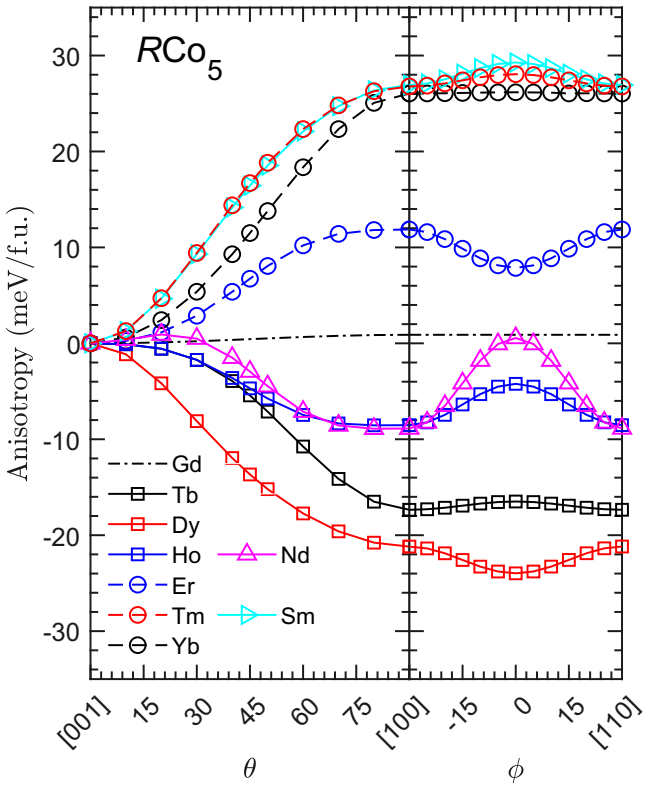

Fig. 2 | Variation of magnetic energy (in meV/f.u.) calculated in DFT+U as a function of spin-axis rotation in RCo_5 with R = Gd, Tb, Dy, Ho, Er, Tm, Yb, Sm, and Nd. The spin direction is characterized by the polar angle θ and the azimuthal angle ϕ. The lattice vector c ([0 0 1]) direction is along the $\hat{z}$ direction and is denoted by $\theta = 0°$, while the lattice vector a ([1 0 0]) direction is denoted by $\theta = 90°$ and $\phi = -30°$. The calculations are performed in DFT+U with $U = 10$ eV on the 4f states of all R elements to satisfy Hund's rules. For all the depicted compounds, the calculated easy directions are consistent with experimental observations.

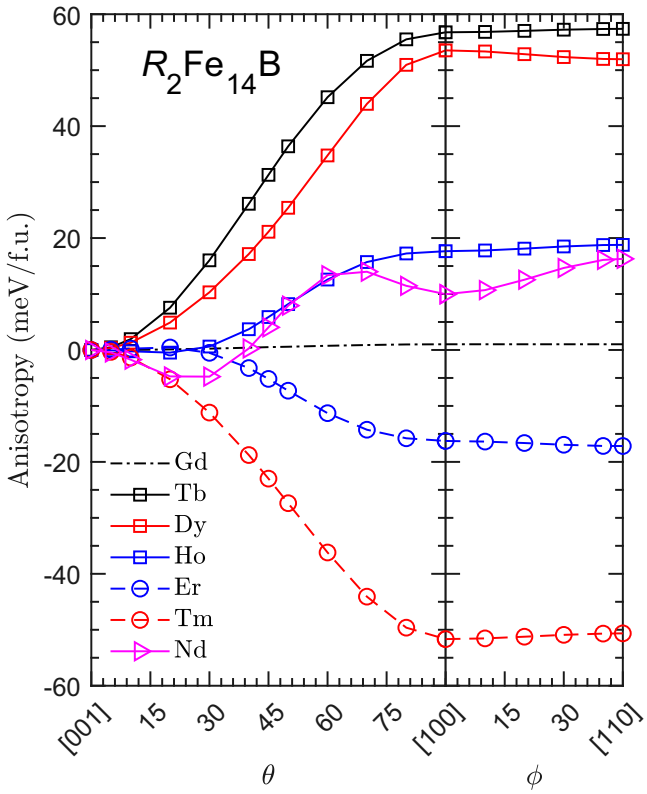

Fig. 3 | Variation of magnetic energy (in meV/f.u.) calculated in DFT+U as a function of spin-axis rotation in $R_2Fe_{14}B$ with R = Gd, Tb, Dy, Ho, Er, Tm, and Nd. The spin direction is characterized by the polar angle θ and the azimuthal angle ϕ. The lattice vector c ([0 0 1]) direction is along the $\hat{z}$ direction and denoted by $\theta = 0°$, while the lattice vector a ([1 0 0]) direction is denoted by $\theta = 90°$ and $\phi = 0°$. The calculations are performed in DFT+U with $U = 8$ eV on the 4f states of all R elements to satisfy Hund's rules. For all the depicted compounds, the calculated easy directions are consistent with experimental observations.

in-plane MA also reflects a difference between the many-body treatment and the single-Slater-determinant description of DFT for the Sm ion.

$R_2Fe_{14}B$ compounds. $R_2Fe_{14}B$ compounds crystallize in a tetragonal crystal structure with space group $P4_2/mnm$ (no. 136). There are two inequivalent R sites, denoted by Wyckoff sites 4g and 4f. The primitive cell consists of four formula units. Experimentally, the easy directions of $R_2Fe_{14}B$ at low temperatures are easy-axial for Tb and Dy, conical for Ho and Nd, and easy-plane for Er and Tm[60].

Figrue 3 shows the MA calculated in $R_2Fe_{14}B$ with the spin quantization direction rotating from [001] to [100] and then to [110] directions of the tetragonal crystal structure. The calculated easy directions again all agree with experimental observations. Notably, for the in-plane MA, $R_2Fe_{14}B$ compounds show somewhat smaller values than those in RCo_5.

Remarkably, very strong easy-axis MA is obtained for R=Tb and Dy. In fact, in practice, a small amount of these two heavy R elements is often required to enhance the coercivities of $R_2Fe_{14}B$-based magnets for real applications. Similar to RCo_5 and RMn_6Sn_6, the calculated $E(\theta, \phi)$ profiles of $R_2Fe_{14}B$ also exhibit perfect particle-hole symmetry for R = Ho and Er.

Experimentally, it was found that the net magnetization in $Nd_2Fe_{14}B$ cants away from the c axis toward the [110] direction by an angle of $\theta = 30°$, measured at 4 K. This is consistent with the calculated energy minimum occurring at $\theta = 30°$ when the spin rotates from [001] to [100], as shown in Fig. 3 We further confirm that rotation from [001] toward [110] produces a slightly deeper energy minimum at $\theta = 30°$ (not shown), thus reproducing exactly the experimental easy-cone angle. The contribution from the two inequivalent Nd sites to the MA is also of great interest. It has been argued that the 4f and 4g sites have negative and positive contributions, respectively, to the MAE[61]. However, we found that contributions from both sites show an energy minimum near $\theta = 30°$ (see Supplementary Fig. 1).

It is interesting that in some light-R elements, DFT—despite being an approximation that projects the Hund's-rules ground state onto a dominant single Slater determinant—successfully reproduces the easy magnetization directions in $SmCo_5$ and $NdCo_5$, as well as the nontrivial easy-cone angle of $Nd_2Fe_{14}B$. We see here that simply enforcing Hund's rules already gives the correct easy direction, an improvement over conventional DFT+U. However, the magnitude of the MAE can be significantly overestimated for light rare earths, such as the easy-axis anisotropy in $SmCo_5$ and the in-plane anisotropy in $NdCo_5$. These errors can be corrected by explicitly accounting for multiple Slater determinants (this will be the subject of a future publication).

RFe_{12} compounds. Fe-rich RFe_{12}-based compounds have recently attracted significant interest in the permanent magnet community[62]. In general, these compounds typically form as $RFe_{12-x}M_x$, requiring a third element M = Ti, V, Cr, Mn, Mo, W, Al, or Si to stabilize a body-centered tetragonal $ThMn_{12}$-type ($I4/mmm$ space group, no. 139) structure. Experimental easy-axis information for $RFe_{11}Ti$ is available for comparison, though there are some disagreements in experimental reports[60,63–65]. For example, both easy-plane and easy-cone MA have been reported for R = Tb, while both easy-axis and easy-cone MA have been reported for R = Ho at low temperatures.

To compare with experiments, we calculated the MA in the hypothetical composition of RFe_{12}, ignoring the third element for simplicity. We found that the calculated MAE per R atom of RFe_{12} is more than five times smaller than in RCo_5 and $R_2Fe_{14}B$. The calculated MA, as showin

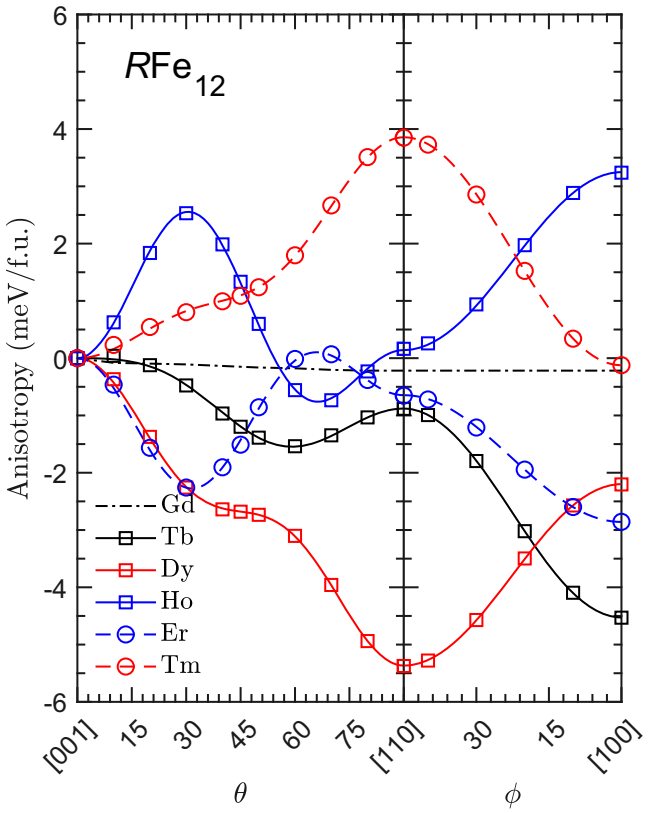

Fig. 4 | Variation of magnetic energy (in meV/f.u.) calculated in DFT+U as a function of spin-axis rotation in RFe$_{12}$ with R = Tb, Dy, Ho, Er, Tm. The spin direction is characterized by the polar angle θ and the azimuthal angle ϕ. The lattice vector c ([0 0 1]) direction is along the $\hat{z}$ direction and denoted by $\theta = 0°$, while the lattice vector a ([1 1 0]) direction is denoted by $\theta = 90°$ and $\phi = 45°$. The calculations were performed using DFT+U with U = 10 eV applied to the 4f states of all R elements, with Hund's rules enforced on the 4f states.

in Fig. 4, is easy-plane for R = Tb and Dy, and easy-cone for R = Ho, which agrees with the experimental findings reported[60,63]. For R = Er and Tm, however, our calculated easy directions for RFe$_{12}$ do not exactly match the experimental results for RFe$_{11}$Ti. Experiments found that the MA is easy-cone and easy-axis, respectively, for R = Er and Tm in RFe$_{11}$Ti. In contrast, for R = Er, our calculations indicate a local minimum at the experimental easy direction, but the energy is slightly higher than that of the in-plane direction. Similarly, for R = Tm, the easy-axis and in-plane directions have nearly identical energies. The discrepancy is likely due to the presence of the Ti atom in the real materials; the chemical effect and induced crystal structure distortion can modify the crystal field of the R element and MA[66]. More comprehensive experiments and MA calculations, incorporating more realistic experimental structures and compositions, are desired to further elucidate MA in RFe$_{12}$-based systems.

***R*Mn$_6$Sn$_6$ and *R*V$_6$Sn$_6$ compounds.** Besides these three permanent magnet systems, we have also previously investigated the rare-earth MA in RMn$_6$Sn$_6$ and RV$_6$Sn$_6$ compounds[6,27], which have recently garnered significant attention as platforms for topological magnets. For all of these different isostructural series, the calculated easy directions are consistent with experiments, as long as reliable experimental measurements are available for comparison. Among these two dozen compounds, in addition to the easy-axis and easy-plane anisotropy, some of them exhibit non-trivial easy-cone angles, e.g., ~ 30° in Nd$_2$Fe$_{14}$B and ~ 45° in DyMn$_6$Sn$_6$ and HoMn$_6$Sn$_6$. Moreover, we found that not only the easy directions but also the magnitudes of MA are comparable to existing experiments[26,27,67]. Therefore, our benchmarking of MA in all of these systems validates the usefulness of applying simplistic DFT+U total energy calculations to investigate rare-earth MA, provided that Hund's rules are enforced.

4*f* anisotropy: Perturbation theory for fast scanning

Perturbation theory (PT) on top of magnetic force theory has been widely used to calculate and spatially resolve MA in non-4f systems, providing a microscopic understanding of MA. Since SOC is much smaller than the CF in d-electron systems and is treated as a perturbation, one obtains $K = \frac{1}{2}K_{SO}$ according to second-order perturbation theory[7,8,68]. In other words, the total MA is half of the anisotropy of the SOC energy, K_{SO}. Unlike total MA, K_{SO} can be resolved into sites, orbitals, spin channels, and bandfillings[7,8,69].

In contrast to d-electron systems, in heavy R systems, CF is much smaller than SOC and should be treated as a perturbation. When the spin rotates, the 4f charge is locked to the spin by the dominant SOC and rotates rigidly with the spin. As a result, the SOC energy E_{SO} remains the same during the rotation, and the MA, in principle, can be calculated as $K = K_{CF}$ in first-order perturbation theory.

The challenge lies in the accurate estimation of CF energy in open-4f-shell elements using DFT+U methods, where CF is overestimated by an order of magnitude, as the aspherical 4f charge induces a much larger CF splitting than the ligands. A quick and rough fix is to use the CF levels of isostructural compounds with R = Gd (f^7), whose half-filled 4f orbitals give a spherical charge and minimize the CF splitting caused by 4f electrons themselves. It is worth noting that, in a similar spirit, Yttrium (f^0) analogues of rare-earth/transition-metal magnets have been used to investigate their CFPs[70,71]. However, for our approach, Gd is better suited for estimating the CF splittings in magnetic rare earths because the occupied 4f states are significantly more localized than the unoccupied ones. Using the occupied 4f levels in Gd provides a much more accurate estimate compared to relying on the high-lying 4f bands of Y.

Obviously, one should expect that the ligand-only-induced CF splittings would vary across the R series, deviating from the values in the Gd counterpart. However, even with this rough estimation of CF, we have shown that the perturbation treatment of 4f MA provides a good description of MA in RMn$_6$Sn$_6$[6]. To further demonstrate the validity of PT application on rare-earth anisotropy, we next model the 4f uniaxial MA in RCo$_5$ and compare it with the 4f-only contributions obtained from total energy calculations.

Figure 5 compares the 4f MA calculated using total energy in DFT and CF energy in PT. The latter is calculated using:

$$E(\theta,\phi) = \sum_{m\in \text{Occ. } 4f} \langle \Psi_m^{\theta,\phi} | H_{CF} | \Psi_m^{\theta,\phi} \rangle. \quad (10)$$

Here, $E_{CF}(\theta,\phi)$ is obtained by evaluating the original CF Hamiltonian in the rotated wavefunctions, or, equivalently, the rotated CF Hamiltonian by $(-\theta,-\phi)$ in the original wavefunctions. For all R elements, we use the CF levels of GdCo$_5$ at Γ, obtained from scalar-relativistic DFT+U calculations. Due to the high symmetry of the RCo$_5$ crystal structure, the H_{CF} is diagonal in the real-spherical-harmonics basis at Γ. Therefore, the eigenvalues of the seven occupied 4f states at Γ in GdCo$_5$ are sufficient to construct the Hamiltonian H_{CF} in the complex-harmonics basis, which serves as the natural basis for the SOC Hamiltonian. The rotated wavefunctions and Hamiltonian can be calculated using the Wigner rotation matrix.

Given that the PT model assumes the Gd-4f crystal field splitting for all R compounds, the agreement between the DFT and PT model is quite reasonable. Notably, the deviation increases from Tb to Yb as one moves farther away from Gd. Our results further demonstrate the validity of the PT approach in describing rare-earth MA.

Due to its simplicity, such PT calculations can be used for 1) fast screening of MA and 2) for understanding the origin of rare-earth MA in a system. For example, large easy-axis MA is required for many applications, such as permanent magnets and topological magnets. Total energy calculations are more demanding, and special care must be taken to ensure

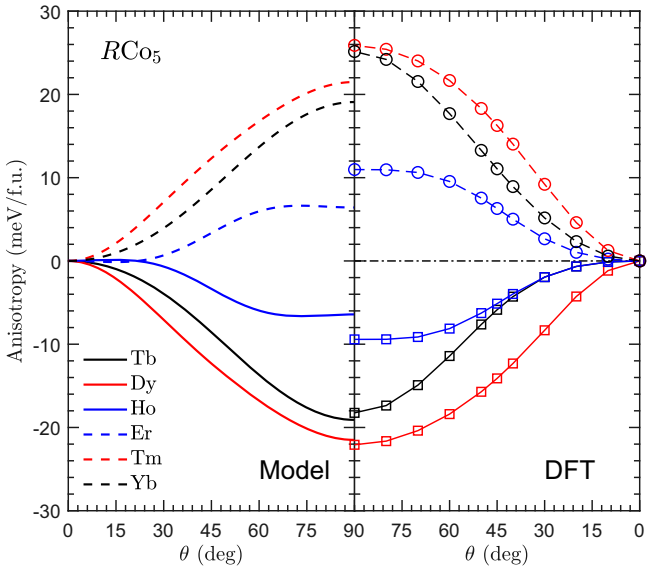

Fig. 5 | Single-ion anisotropy of *R*-4*f* in RCo_5 calculated using the perturbation model and DFT+*U*. The anisotropy is represented as a function of the spin quantization angle, characterized by the polar angle θ, in RCo_5, modeled with perturbation theory using CF levels from $GdCo_5$. The CF levels of $GdCo_5$ are calculated using DFT+*U* without SOC, with $U \approx 10$ eV. In this analysis, the energy difference between the $|m_l = \pm 3\rangle$ 4*f* levels is disregarded, as it reflects in-plane anisotropy but not uniaxial anisotropy.

convergence to the desired 4*f* configurations at every spin direction. In this context, before conducting more reliable total energy calculations, PT calculations can be used for a rapid initial screening of rare-earth MA to identify potential easy-axis rare-earth MA in unexplored crystal structures. Furthermore, the PT approach can be used to decompose MA contributions into those from different rare-earth sites, such as in $R_2Fe_{14}B$, and analyze how the MA changes with other tuning parameters, thereby aiding in the understanding of the origin of MA in a system.

Discussion

In summary, using $TbMn_6Sn_6$, we illustrate a general challenge of calculating rare-earth magnetocrystalline anisotropy in DFT and related methods, which often fail to reproduce the correct Hund's-rules ground state of rare-earth elements due to significant orbital dependence of the self-interaction error for strongly localized 4*f* orbitals, and the lack of explicit proper orbital polarization treatment. The true ground state appears as a metastable state that lies several hundred meV above, resulting in an incorrect 4*f* orbital occupation associated with an incorrect 4*f* charge density, which in turn leads to incorrect magnetocrystalline anisotropy. However, as the self-interaction error and orbital polarization are, in principle, largely rotationally invariant, the anisotropy of the true ground state might be expected to remain correct if Hund's rules are enforced by hand.

We have benchmarked this approach on materials with rare-earth atoms with saturated moments where Hund's rules are expected to be satisfied and the single Slater determinant description is suitable. Notably, in RCo_5, $R_2Fe_{14}B$, RFe_{12}, and other compounds, the calculated easy directions (including easy axes, planes, and conical angles) have all agreed resonablly well with low-temperature measurements.

Besides total energy calculations, we also demonstrate the application of perturbation theory for evaluating rare-earth anisotropy. The good agreement between the perturbation approach and total energy calculations shows that it can be a useful tool for fast screening of new systems. Moreover, in analogy to using the SOC anisotropy to spatially resolve 3*d* anisotropy, such perturbation treatment of crystal field energy can be used to resolve anisotropy in systems that contain multiple nonequivalent rare-earth sites, aiding in the understanding the microscopic origin of rare-earth anisotropy.

Methods

Total energy calculations of magnetocrystalline anisotropy

To evaluate the MA, we use DFT to compute the total energies $E(\theta, \phi)$ as a function of the spin-quantization direction, characterized by the polar angle θ and the azimuthal angle ϕ. Unlike anisotropy in 3*d*-electron systems, where SOC is generally much weaker than CF and can be treated as a perturbation—allowing the use of the force theorem for MAE calculations—fully self-consistent DFT+*U*+SOC calculations with various spin directions are required to compute the MA of 4*f* systems. Additionally, the Hund's rule states are enforced for all spin quantization directions in all rare-earth elements.

Crystal structure

Experimental crystal structures were used for all calculations. Detailed structural parameters, including lattice constants, atomic positions, and corresponding references, are provided in Supplementary Tables S1, S2 and S3. Note that RFe_{12} is a hypothetical compound, as real compounds always contain a small amount of a third element, such as in $RFe_{11}Ti$, to stabilize the structure.

DFT+*U*+SOC calculation details

The DFT calculations were performed using the full-potential linear augmented plane wave (FP-LAPW) method, as implemented in WIEN2K[72]. The generalized gradient approximation (GGA) of Perdew, Burke, and Ernzerhof[73] was used for the exchange and correlation potentials.

The strongly correlated *R*-4*f* electrons were treated using the DFT+*U* method with the fully localized limit (FLL) double-counting scheme[19]. Sizable *U* values (8–10 eV) were employed to shift the occupied 4*f* states away from the Fermi level. SOC was included using the second-variational method[74–76]. Compared to the scalar-relativistic case, SOC explicitly couples the spin-up and spin-down channels and reduces the symmetry.

To generate the self-consistent potential and charge, we employed $R_{MT} \cdot K_{max} = 9$, 8, and 9 for RCo_5, $R_2Fe_{14}B$, and RFe_{12}, respectively, with muffin-tin radii R_{MT} = 2.8, 2.1, 2.1, and 1.6 a.u. for *R*, Fe, Co, and B atoms, respectively. The calculations were performed with 7200, 400, and 4800 *k*-points in the full Brillouin zone (FBZ) for RCo_5, $R_2Fe_{14}B$, and RFe_{12}, respectively. A further increase in the number of *k*-points had a negligible effect on the results. For *k*-space integrations to determine the Fermi level, the tetrahedron integration method with Blöchl corrections[77] was used. The calculations were iterated until the charge difference between consecutive iterations was smaller than $10^{-5}e$ and the total energy difference was below 10^{-3} mRy/cell.

For perturbation modeling, the CF levels of Gd-4*f* states of corresponding Gd-containing compounds are calculated without SOC in DFT +*U* and used for all *R* elements. Therefore, our perturbation model ignore the dependence of the CF on *R* elements. Additionally, we performed MA calculations for corresponding Gd compounds (or treated 4*f* as a spherical open-core) to obtain the non-4*f* contributions to the total MA[6].

Enforcing Hund's Rule for the 4*f* States: with and without constraints

To enforce the Hund's rule state for 4*f* electrons, we performed DFT+*U* +SOC calculations with constraints. Specifically, we initialized and then froze the 4*f* occupancy matrix (and consequently, the potentials dependent on it) for each spin direction until the system reached convergence.

Once self-consistency was achieved, the constraint could be lifted, allowing additional iterations to fully relax the 4*f* states near the targeted Hund's rule states. With sizable *U* values of 8–10 eV, the Hund's rule state solution remained stable even after the constraint was removed. Special care, such as reducing the mixing parameters, was sometimes required to ensure that the solution remained in the designated state during subsequent iterations after the constraint was lifted, which could result in a slow process.

However, key results, including magnetic moments and anisotropy, remained nearly unchanged when comparing the constrained and relaxed cases (See Supplementary Discussions for details). Therefore, we primarily report the constrained calculations in this work. On the other hand, for small

U values, the constraint often became necessary and could not be removed. Some 4*f* configurations can become extremely difficult—or even impossible—to stabilize without a constraint, as strong hybridization could destabilize the targeted states.

Data availability

The data that support the findings of this study are available from the corresponding author upon reasonable request.

Received: 15 July 2024; Accepted: 1 April 2025;
Published online: 05 June 2025

References

1. Gschneidner, K. A. & Eyring, L. (eds.) *Handbook on the Physics and Chemistry of Rare Earths* (North Holland, Amsterdam, 1978).
2. Schüler, K. Mccaig: Permanent magnets in theory and practice. *Physikalische Bl.ätter* **35**, 423 (1979).
3. Lewis, L. H. & Jiménez-Villacorta, F. Perspectives on permanent magnetic materials for energy conversion and power generation. *Metall. Mater. Trans. A* **44**, 20–44 (2013).
4. McCallum, R., Lewis, L., Skomski, R., Kramer, M. & Anderson, I. Practical aspects of modern and future permanent magnets. *Annu. Rev. Mater. Res.* **44**, 451–477 (2014).
5. Yin, J.-X. et al. Quantum-limit Chern topological magnetism in $TbMn_6Sn_6$. *Nature* **583**, 533–536 (2020).
6. Lee, Y. et al. Interplay between magnetism and band topology in the kagome magnets RMn_6Sn_6. *Phys. Rev. B* **108**, 045132 (2023).
7. Ke, L. & van Schilfgaarde, M. Band-filling effect on magnetic anisotropy using a Green's function method. *Phys. Rev. B* **92**, 014423 (2015).
8. Ke, L. Intersublattice magnetocrystalline anisotropy using a realistic tight-binding method based on maximally localized Wannier functions. *Phys. Rev. B* **99**, 054418 (2019).
9. Hutchings, M. Point-Charge Calculations of Energy Levels of Magnetic Ions in Crystalline Electric Fields. vol. 16 of *Solid State Physics*, 227–273 (Academic Press, 1964).
10. Taylor, K. N. R. & Darby, M. I. *Physics of rare earth solids* (Chapman and Hall, London, 1972).
11. Skomski, R. & Coey, J. M. D. *Permanent magnetism* (Institute of Physics Publishing, Bristol, 1999).
12. Jensen, J. & Mackintosh, A. R. *Rare earth magnetism* (Clarendon Press Oxford, 1991).
13. Peters, L. et al. Treatment of 4*f* states of the rare earths: The case study of TbN. *Phys. Rev. B* **89**, 205109 (2014).
14. Locht, I. L. M. et al. Standard model of the rare earths analyzed from the Hubbard I approximation. *Phys. Rev. B* **94**, 085137 (2016).
15. Liechtenstein, A. I., Anisimov, V. I. & Zaanen, J. Density-functional theory and strong interactions: Orbital ordering in Mott-Hubbard insulators. *Phys. Rev. B* **52**, R5467–R5470 (1995).
16. Delange, P., Biermann, S., Miyake, T. & Pourovskii, L. Crystal-field splittings in rare-earth-based hard magnets: An ab initio approach. *Phys. Rev. B* **96**, 155132 (2017).
17. Pourovskii, L. V., Boust, J., Ballou, R., Eslava, G. G. & Givord, D. Higher-order crystal field and rare-earth magnetism in rare-earth–Co_5 intermetallics. *Phys. Rev. B* **101**, 214433 (2020).
18. Chantis, A. N., van Schilfgaarde, M. & Kotani, T. Quasiparticle self-consistent *GW* method applied to localized 4*f* electron systems. *Phys. Rev. B* **76**, 165126 (2007).
19. Anisimov, V. I., Solovyev, I. V., Korotin, M. A., Czyżyk, M. T. & Sawatzky, G. A. Density-functional theory and NiO photoemission spectra. *Phys. Rev. B* **48**, 16929–16934 (1993).
20. Czyżyk, M. T. & Sawatzky, G. A. Local-density functional and on-site correlations: The electronic structure of La_2CuO_4 and $LaCuO_3$. *Phys. Rev. B* **49**, 14211–14228 (1994).
21. Solovyev, I. V., Dederichs, P. H. & Anisimov, V. I. Corrected atomic limit in the local-density approximation and the electronic structure of *d* impurities in Rb. *Phys. Rev. B* **50**, 16861–16871 (1994).
22. Shick, A. B., Liechtenstein, A. I. & Pickett, W. E. Implementation of the LDA+U method using the full-potential linearized augmented plane-wave basis. *Phys. Rev. B* **60**, 10763–10769 (1999).
23. Singh, D. J. & Nordstrom, L. *Planewaves, Pseudopotentials, and the LAPW method* (Springer Science & Business Media, 2006).
24. Zhou, F. & Ozoliņš, V. Obtaining correct orbital ground states in *f*-electron systems using a nonspherical self-interaction-corrected LDA $+U$ method. *Phys. Rev. B* **80**, 125127 (2009).
25. Gotsis, H. J. & Mazin, I. I. Ferromagnetism and spin-orbital compensation in Sm intermetallics. *Phys. Rev. B* **68**, 224427 (2003).
26. Riberolles, S. X. M. et al. Low-Temperature Competing Magnetic Energy Scales in the Topological Ferrimagnet $TbMn_6Sn_6$. *Phys. Rev. X* **12**, 021043 (2022).
27. Rosenberg, E. et al. Uniaxial ferromagnetism in the kagome metal TbV_6Sn_6. *Phys. Rev. B* **106**, 115139 (2022).
28. Note. It is worth noting that the *exact* dft is still a single-determinant method, yet it can describe MA. Theoretically, this is achieved through the kohn-sham wave functions that deviate from standard spherical harmonics in the single determinant. Personal note (2024).
29. Allen, J. P. & Watson, G. W. Occupation matrix control of *d*- and *f*-electron localisations using DFT + U. *Phys. Chem. Chem. Phys.* **16**, 21016–21031 (2014).
30. Janesko, B. G. Unification of Perdew-Zunger self-interaction correction, DFT+*U*, and Rung 3.5 density functionals. *J. Chem. Phys.* **157**, 151101 (2022).
31. Solovyev, I. V., Liechtenstein, A. I. & Terakura, K. Is Hund's Second Rule Responsible for the Orbital Magnetism in Solids? *Phys. Rev. Lett.* **80**, 5758–5761 (1998).
32. Zhou, F. & Ozoliņš, V. Self-consistent density functional calculations of the crystal field levels in lanthanide and actinide dioxides. *Phys. Rev. B* **85**, 075124 (2012).
33. Lebègue, S. et al. Electronic structure and spectroscopic properties of thulium monochalcogenides. *Phys. Rev. B* **72**, 245102 (2005).
34. Söderlind, P. et al. Prediction of the new efficient permanent magnet $SmCoNiFe_3$. *Phys. Rev. B* **96**, 100404 (2017).
35. Pourovskii, L. V., Amadon, B., Biermann, S. & Georges, A. Self-consistency over the charge density in dynamical mean-field theory: A linear muffin-tin implementation and some physical implications. *Phys. Rev. B* **76**, 235101 (2007).
36. Perdew, J. P. & Zunger, A. Self-interaction correction to density-functional approximations for many-electron systems. *Phys. Rev. B* **23**, 5048–5079 (1981).
37. Svane, A. & Gunnarsson, O. Localization in the self-interaction-corrected density-functional formalism. *Phys. Rev. B* **37**, 9919–9922 (1988).
38. Zhang, Y. & Yang, W. A challenge for density functionals: Self-interaction error increases for systems with a noninteger number of electrons. *J. Chem. Phys.* **109**, 2604–2608 (1998).
39. Cohen, A. J., Mori-Sánchez, P. & Yang, W. Insights into current limitations of density functional theory. *Science* **321**, 792–794 (2008).
40. Alonso, J. A. & Girifalco, L. A. Nonlocal approximation to the exchange potential and kinetic energy of an inhomogeneous electron gas. *Phys. Rev. B* **17**, 3735–3743 (1978).
41. Mazin, I. I. & Singh, D. J. Nonlocal density functionals and the linear response of the homogeneous electron gas. *Phys. Rev. B* **57**, 6879–6883 (1998).
42. Temmerman, W. et al. Chapter 241 the dual, localized or band like, character of the 4f states. vol. 39 of *Handbook on the Physics and Chemistry of Rare Earths*, 1–112 (Elsevier, 2009).
43. Strange, P., Svane, A., Temmerman, W. M., Szotek, Z. & Winter, H. Understanding the valency of rare earths from first-principles theory. *Nature* **399**, 756–758 (1999).

44. Hughes, I. D. et al. Lanthanide contraction and magnetism in the heavy rare earth elements. *Nature* **446**, 650–653 (2007).
45. Svane, A., Temmerman, W. M., Szotek, Z., Lægsgaard, J. & Winter, H. Self-interaction-corrected local-spin-density calculations for rare earth materials. *Int. J. Quantum Chem.* **77**, 799–813 (2000).
46. Lüders, M. et al. Self-interaction correction in multiple scattering theory. *Phys. Rev. B* **71**, 205109 (2005).
47. Patrick, C. E. & Staunton, J. B. Rare-earth/transition-metal magnets at finite temperature: Self-interaction-corrected relativistic density functional theory in the disordered local moment picture. *Phys. Rev. B* **97**, 224415 (2018).
48. Eriksson, O., Brooks, M. S. S. & Johansson, B. Orbital polarization in narrow-band systems: Application to volume collapses in light lanthanides. *Phys. Rev. B* **41**, 7311–7314 (1990).
49. Eschrig, H., Sargolzaei, M., Koepernik, K. & Richter, M. Orbital polarization in the Kohn-Sham-Dirac theory. *Europhys. Lett.* **72**, 611 (2005).
50. Daalderop, G. H. O., Kelly, P. J. & Schuurmans, M. F. H. Magnetocrystalline anisotropy of YCo_5 and related $RECo_5$ compounds. *Phys. Rev. B* **53**, 14415–14433 (1996).
51. Ke, L., Kukusta, D. A. & Johnson, D. D. Origin of magnetic anisotropy in doped Ce_2Co_{17} alloys. *Phys. Rev. B* **94**, 144429 (2016).
52. Steinbeck, L., Richter, M. & Eschrig, H. Magnetocrystalline anisotropy of RCo_5 intermetallics: itinerant-electron contribution. *J. Magn. Magn. Mater.* **226-230**, 1011–1013 (2001).
53. Zhu, J.-X. et al. LDA+DMFT Approach to Magnetocrystalline Anisotropy of Strong Magnets. *Phys. Rev. X* **4**, 021027 (2014).
54. Kelaeev, V. V., Chuev, V. V., Pibogov, A. N. & Sidoeov, S. K. Anisotropy and Exchange Effects in Heavy Rare-Earth-Cobalt Compounds of the RCo_5 Type. *Phys. status solidi (a)* **79**, 57–66 (1983).
55. Zhao, T., Jin, H., Guo, G., Han, X. & Chen, H. Magnetic properties of R ions in RCo_5 compounds (R=Pr, Nd, Sm, Gd, Tb, Dy, Ho, and Er). *Phys. Rev. B* **43**, 8593–8598 (1991).
56. Skokov, K. et al. Magnetocaloric effect, magnetic domain structure and spin-reorientation transitions in $HoCo_5$ single crystals. *J. Magn. Magn. Mater.* **323**, 447–450 (2011).
57. Larson, P., Mazin, I. I. & Papaconstantopoulos, D. A. Effects of doping on the magnetic anisotropy energy in $SmCo_{5-x}Fe_x$ and $YCo_{5-x}Fe_x$. *Phys. Rev. B* **69**, 134408 (2004).
58. Ermolenko, A. Magnetocrystalline anisotropy of rare earth intermetallics. *IEEE Trans. Magn.* **12**, 992–996 (1976).
59. Ermolenko, A. S. Exchange interactions and magnetocrystalline anisotcopy of rare-earth-cobalt compounds with $CaCu_5$-type structure. *Phys. status solidi (a)* **59**, 331–339 (1980).
60. Szytula, A. & Leciejewicz, J.*Handbook of Crystal Structures and Magnetic Properties of Rare Earth Intermetallics* (CRC Press, 1994).
61. Haskel, D. et al. Atomic origin of magnetocrystalline anisotropy in $Nd_2Fe_{14}B$. *Phys. Rev. Lett.* **95**, 217207 (2005).
62. Ke, L. & Johnson, D. D. Intrinsic magnetic properties in $R(Fe_{1-x}Co_x)_{11}TiZ$ (R=Y and Ce; Z=H, C, and N). *Phys. Rev. B* **94**, 024423 (2016).
63. Boltich, E. et al. Spin reorientations in $RTiFe_{11}$ systems (R = Tb, Dy and Ho). *J. Magn. Magn. Mater.* **78**, 364–370 (1989).
64. Kou, X. C. et al. Magnetic phase transitions, magnetocrystalline anisotropy, and crystal-field interactions in the $RFe_{11}Ti$ series (where R=Y, Pr, Nd, Sm, Gd, Tb, Dy, Ho, Er, or Tm). *Phys. Rev. B* **47**, 3231–3242 (1993).
65. Hu, B.-P., Li, H.-S., Gavigan, J. P. & Coey, J. M. D. Intrinsic magnetic properties of the iron-rich $ThMn_{12}$-structure alloys $R(Fe_{11}Ti)$; R=Y, Nd, Sm, Gd, Tb, Dy, Ho, Er, Tm and Lu. *J. Phys.: Condens. Matter* **1**, 755 (1989).
66. Patrick, C. E., Huang, Y., Lewis, L. H. & Staunton, J. B. Theory of defect-induced crystal field perturbations in rare-earth magnets. *Phys. Rev. Lett.* **132**, 056703 (2024).
67. Pokharel, G. et al. Highly anisotropic magnetism in the vanadium-based kagome metal TbV_6Sn_6. *Phys. Rev. Mater.* **6**, 104202 (2022).
68. Antropov, V., Ke, L., & Aberg, D. Constituents of magnetic anisotropy and a screening of spin-orbit coupling in solids. *Solid State Commun.* **194**, 35–38 (2014).
69. Belashchenko, K. D. et al. Origin of the spin reorientation transitions in $(Fe_{1-x}Co_x)_2B$ alloys. *Appl. Phys. Lett.* **106**, 062408 (2015).
70. Patrick, C. E. & Staunton, J. B. Crystal field coefficients for yttrium analogues of rare-earth/transition-metal magnets using density-functional theory in the projector-augmented wave formalism. *J. Phys.: Condens. Matter* **31**, 305901 (2019).
71. Patrick, C. E. & Staunton, J. B. Temperature-dependent magnetocrystalline anisotropy of rare earth/transition metal permanent magnets from first principles: The light RCo_5(R = Y, La-Gd) intermetallics. *Phys. Rev. Mater.* **3**, 101401 (2019).
72. Blaha, P. et al. *WIEN2k: An Augmented Plane Wave plus Local Orbitals Program for Calculating Crystal Properties* (Vienna University of Technology, Austria, 2018).
73. Perdew, J. P., Burke, K. & Ernzerhof, M. Generalized Gradient Approximation Made Simple. *Phys. Rev. Lett.* **77**, 3865–3868 (1996).
74. Koelling, D. D. & Harmon, B. N. A technique for relativistic spin-polarised calculations. *J. Phys. C: Solid State Phys.* **10**, 3107 (1977).
75. Li, C., Freeman, A. J., Jansen, H. J. F. & Fu, C. L. Magnetic anisotropy in low-dimensional ferromagnetic systems: Fe monolayers on Ag(001), Au(001), and Pd(001) substrates. *Phys. Rev. B* **42**, 5433–5442 (1990).
76. Shick, A. B., Novikov, D. L. & Freeman, A. J. Relativistic spin-polarized theory of magnetoelastic coupling and magnetic anisotropy strain dependence: Application to Co/Cu(001). *Phys. Rev. B* **56**, R14259–R14262 (1997).
77. Blöchl, P. E., Jepsen, O. & Andersen, O. K. Improved tetrahedron method for Brillouin-zone integrations. *Phys. Rev. B* **49**, 16223–16233 (1994).

Acknowledgements

L.K. gratefully acknowledges discussions with the late Ralph Skomski. The work at Ames National Laboratory is supported by the U.S. Department of Energy (USDOE), Office of Basic Energy Sciences, Division of Materials Sciences and Engineering. The initial work by L.K. were supported by the USDOE Early Career Research Program. Ames National Laboratory is operated for the U.S. Department of Energy by Iowa State University under Contract No. DE-AC02-07CH11358. IIM acknowledges support from the National Science Foundation under Award No. DMR-2403804.

Author contributions

L.K. conceived and designed the study. Y.L., Z.N., and L.K. performed the ab initio calculations and model analysis. R.F., R.J.M., and I.I.M contributed to the discussion and analysis of the results. All authors participated in the discussion, writing, and editing of the final manuscript.

Competing interests

The authors declare no competing interests.

Additional information

Supplementary information The online version contains supplementary material available at https://doi.org/10.1038/s41524-025-01632-3.

Correspondence and requests for materials should be addressed to Liqin Ke.